Center for Turbulence Research
Annual Research Briefs 1992

Large-eddy simulation of turbulent flow with a surface-mounted two-dimensional obstacle

By Kyung-Soo Yang[1] AND Joel H. Ferziger[1]

1. Motivation and objectives

Large-eddy simulation (LES) is an accurate method of simulating complex turbulent flows in which the large flow structures are computed while small scales are modeled. The rationale behind this method is based on two observations: most of the turbulent energy is in the large structures, and the small scales are more isotropic and universal. Therefore, LES may be more general and less geometry-dependent than Reynolds-averaged modeling, although it comes at higher cost.

Even though LES has been used by many investigators, most research has been limited to flows with simple geometry. Here we shall consider a rectangular parallelopiped mounted on a flat surface. Related flows are those over surfaces protruding from submarines (conning towers or control fins), wind flows around buildings, and air flows over computer chips, among others. The most distinctive features associated with these flows are three dimensionality, flow separation due to protruding surfaces, and large scale unsteadiness. As a model flow, we consider a plane channel flow in which a two-dimensional obstacle is mounted on one surface (see Fig. 1). This relatively simple geometry contains flow separation and reattachment. Flow in this geometry has been studied by Tropea & Gackstatter (1985) for low Re and Werner & Wengle (1989) and Dimaczek, Kessler, Martinuzzi & Tropea (1989) for high Re, among others.

Recently, Germano, Piomelli, Moin & Cabot (1991) suggested a dynamic subgrid-scale model in which the model coefficient is dynamically computed as computation progresses rather than input *a priori*. This approach is based on an algebraic identity between the subgrid-scale stresses at two different filter levels and the resolved turbulent stresses. They applied the model to transitional and fully turbulent channel flows and showed that the model contributes nothing in laminar flow and exhibits the correct asymptotic behavior in the near-wall region of turbulent flows without an *ad hoc* damping function. This is a significant improvement over conventional subgrid-scale modeling.

Until very recently, use of the dynamic model in complex geometries has been difficult owing to the lack of homogeneous directions over which to average the model coefficient (see Ghosal *et al.* this volume for a dynamic model applicable to inhomogeneous flows). The present work was accomplished prior to the developments of Ghosal *et al.* and accordingly makes use of a combination of time and spatial averages in order to determine the model coefficient. The averaging scheme will be discussed in more detail in §3.

1 Stanford University

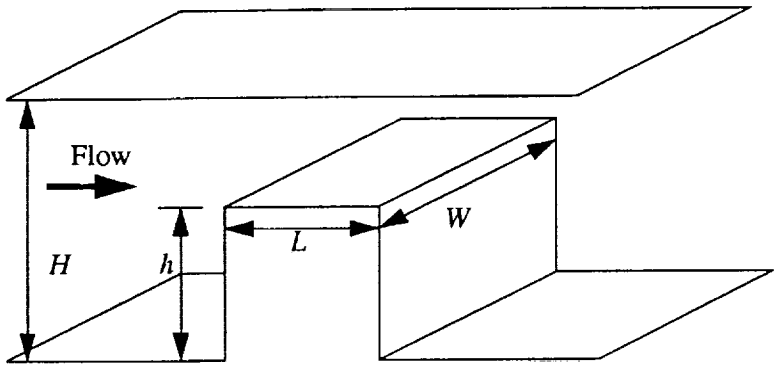

FIGURE 1. Physical configuration.

In this paper, we perform an LES of turbulent flow in a channel containing a two-dimensional obstacle on one wall using a dynamic subgrid-scale model (DSGSM) at Re=3210, based on bulk velocity above the obstacle (U_m) and obstacle height (h); the wall layers are fully resolved. The low Re enables us to perform a DNS (Case I) against which to validate the LES results. The LES with the DSGSM is designated Case II. In addition, an LES with the conventional fixed model constant (Case III) is conducted to allow identification of improvements due to the DSGSM.

We also include LES at Re=82,000 (Case IV) using conventional Smagorinsky subgrid-scale model and a wall-layer model. The results will be compared with the experiment of Dimaczek *et al.* (1989).

2. Formulation

All variables are nondimensionalized by U_m and h. The code uses a nonuniform Cartesian staggered grid in a finite-volume approach. The incompressible momentum equations filtered by a simple volume-average box filter are

$$\frac{\partial \overline{u}_i}{\partial t} + \frac{\partial}{\partial x_j}(\overline{u_i u_j}) = -\frac{\partial \overline{p}}{\partial x_i} + \frac{1}{Re}\frac{\partial^2 \overline{u}_i}{\partial x_j \partial x_j}, \tag{1}$$

where u_1, u_2, u_3 (or u, v, w) are velocities in x_1 (streamwise), x_2 (normal), x_3 (spanwise) directions (or x, y, z), respectively, and p is pressure. The volume-average box filter is defined by

$$\overline{u}_i(\vec{x},t) = \frac{1}{\Delta x_1 \Delta x_2 \Delta x_3}\int_{x_1-\frac{\Delta x_1}{2}}^{x_1+\frac{\Delta x_1}{2}}\int_{x_2-\frac{\Delta x_2}{2}}^{x_2+\frac{\Delta x_2}{2}}\int_{x_3-\frac{\Delta x_3}{2}}^{x_3+\frac{\Delta x_3}{2}} u_i(\vec{x'},t)d\vec{x'}, \tag{2}$$

where $\vec{x}=(x_1,x_2,x_3)$ and $d\vec{x'}=dx'_1dx'_2dx'_3$. The convective term can be rewritten as

$$\frac{\partial}{\partial x_j}(\overline{u_i u_j}) = \frac{\partial}{\partial x_j}(\overline{u}_i\overline{u}_j + L_{ij} + C_{ij} + R_{ij}), \tag{3}$$

where

$$\begin{cases} L_{ij} = \overline{\overline{u}_i \overline{u}_j} - \overline{u}_i \overline{u}_j \\ C_{ij} = \overline{\overline{u}_i u'_j} + \overline{\overline{u}_j u'_i} \\ R_{ij} = \overline{u'_i u'_j}. \end{cases} \tag{4}$$

L_{ij}, C_{ij}, R_{ij} represent Leonard stresses, cross terms, subgrid-scale Reynolds stresses, respectively. When a finite-difference scheme of second-order accuracy is used, the Leonard stresses are of the same order as the truncation error (Shaanan, Ferziger & Reynolds, 1975). The other terms have to be modeled.

The governing equations for LES become

$$\frac{\partial \overline{u}_i}{\partial x_i} = 0, \tag{5}$$

$$\frac{\partial \overline{u}_i}{\partial t} + \frac{\partial}{\partial x_j}(\overline{u}_i \overline{u}_j) = -\frac{\partial P}{\partial x_i} - \frac{\partial}{\partial x_j}\tau_{ij} + \frac{1}{Re}\frac{\partial^2 \overline{u}_i}{\partial x_j \partial x_j}, \tag{6}$$

where

$$\begin{cases} \tau_{ij} = Q_{ij} - \frac{1}{3}Q_{kk}\delta_{ij} \\ P = \overline{p} + \frac{1}{3}Q_{kk} \\ Q_{ij} = R_{ij} + C_{ij}. \end{cases} \tag{7}$$

Here, δ_{ij} is the Kronecker symbol. In the present simulation, the eddy viscosity model of Smagorinsky (1963) is used:

$$\tau_{ij} = -2\nu_T \overline{S}_{ij}, \tag{8}$$

where

$$\begin{cases} \overline{S}_{ij} = \frac{1}{2}\left(\frac{\partial \overline{u}_i}{\partial x_j} + \frac{\partial \overline{u}_j}{\partial x_i}\right) \\ \nu_T = l^2\sqrt{2\overline{S}_{ij}\overline{S}_{ij}}. \end{cases} \tag{9}$$

Here, l is a characteristic length scale of the small eddies. In Case III and IV, the smaller value of κd and $0.1\overline{\Delta}$ is used for l, where κ and d are von Karman's constant and the distance normal to a wall, respectively, and $\overline{\Delta} = (\Delta x \Delta y \Delta z)^{\frac{1}{3}}$. The particular form of τ_{ij} in (7) is chosen in order to make both (7) and (8) consistent on contraction ($i = j$).

In Case II, $l^2 = C_s\Delta^2$ is dynamically determined following the prescription of Germano *et al.* (1991) as modified by Lilly (1992). When the dynamic model is used, C_s is an instantaneous and local quantity that can vary wildly in time and space. This wide variation results in large negative values of C_s that lead to numerical instability. To avoid this difficulty, averaging is performed in space and time. (For an alternate approach see Ghosal *et al.*, this volume). Spatial averaging is done in the homogeneous (z) direction first. Then additional averaging is performed over nine neighboring grid points with the point for which the averaging is carried out at the center, using volume weighting, in order to obtain an averaged value of C_s at a given inner grid point. In the near-wall region, averaging is done only in the direction parallel to the solid wall, i.e. using three points. It is necessary to repeat this process to smooth C_s sufficiently. Germano *et al.* (1991) found the optimum value of the ratio, $\widetilde{\overline{\Delta}}/\overline{\Delta}$, to be two, a value we adopted.

3. Numerical method

To advance the solution in time, a fractional step method (Kim and Moin, 1985) is employed. The time-advancement of the momentum equation is hybrid; the convective terms are explicitly advanced by a third-order Runge-Kutta scheme and the viscous terms implicitly by Crank-Nicolson method:

$$\frac{\widehat{\overline{u}}_i^k - \overline{u}_i^{k-1}}{\Delta t} = (\alpha_k + \beta_k) L(\overline{u}_i^{k-1}) + \beta_k L(\widehat{\overline{u}}_i^k - \overline{u}_i^{k-1})$$

$$-\gamma_k N(\overline{u}_i^{k-1}) - \zeta_k N(\overline{u}_i^{k-2}) - (\alpha_k + \beta_k)\frac{\partial \overline{P}^{k-1}}{\partial x_i}, \tag{10}$$

$$\frac{\overline{u}_i^k - \widehat{\overline{u}}_i^k}{\Delta t} = -\frac{\partial \overline{\phi}^k}{\partial x_i} \quad (k = 1, 2, 3), \tag{11}$$

where

$$\frac{\partial \overline{P}^k}{\partial x_i} = \frac{\partial \overline{P}^{k-1}}{\partial x_i} + \left(\frac{1}{\alpha_k + \beta_k} - \frac{\beta_k \Delta t}{\alpha_k + \beta_k} L\right)\frac{\partial \overline{\phi}^k}{\partial x_i},$$

$$L = \frac{1}{Re}\frac{\partial^2}{\partial x_j \partial x_j} + \frac{\partial}{\partial x_j}\nu_T(1 + \delta_{ij})\frac{\partial}{\partial x_j},$$

$$N(\overline{u}_i) = \frac{\partial}{\partial x_j}(\overline{u}_i \overline{u}_j) - \frac{\partial}{\partial x_j}\nu_T(1 - \delta_{ij})\frac{\partial \overline{u}_j}{\partial x_i},$$

with

$$\gamma_1 = \frac{8}{15}, \quad \gamma_2 = \frac{5}{12}, \quad \gamma_3 = \frac{3}{4}, \quad \zeta_1 = 0, \quad \zeta_2 = -\frac{17}{60}, \quad \zeta_3 = -\frac{5}{12},$$

$$\alpha_1 = \beta_1 = \frac{4}{15}, \quad \alpha_2 = \beta_2 = \frac{1}{15}, \quad \alpha_3 = \beta_3 = \frac{1}{6},$$

$$\sum_{k=1}^{3}(\alpha_k + \beta_k) = \sum_{k=1}^{3}(\gamma_k + \zeta_k) = 1.$$

In the expressions for L and $N(\overline{u}_i)$, summation is performed on the index j only. The momentum equation is time-advanced without implicit pressure terms and then projected onto a divergence-free space by introducing $\overline{\phi}$ that obeys a Poisson equation. The latter is solved by a multigrid method which is very flexible and more efficient than a number of competitors. For spatial discretization, second-order accurate central differencing was used. All terms in the model except the cross derivatives are treated implicitly in all three directions to avoid restrictions on time steps. The code is well vectorized; a speed of 150 MFLOPS has been achieved on CRAY Y-MP/832.

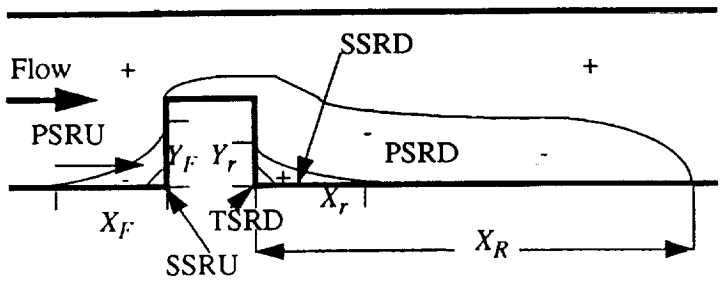

FIGURE 2. Schematic drawing of SR regions.

Case	Re	X_R	X_r	Y_r	X_F	Y_F
I	3310	6.42	1.21	0.35	1.51	0.28
II	3210	6.80	1.13	0.36	1.51	0.37
III	3330	7.01	1.76	0.28	1.35	0.40

Table 1. Comparison of various SR lengths.

4. Results and discussion

4.1 Choice of parameters and boundary conditions

The values of the geometric parameters in all four cases are h/H=0.5, W/h=2, and L/h=1, where H, W, and L are channel height, spanwise width of the obstacle and channel, and obstacle streamwise length, respectively (see Fig. 1). The inlet and the outlet are located at x=0 and x=31, respectively, and the obstacle is placed between x=10 and x=11.

In Cases II and III the center of the control volume adjacent to the wall was placed at Δy=0.0086 from horizontal walls except on the top of the obstacle where the nearest center was placed at Δy=0.0046. The corresponding distances for Case I and Case IV are 0.005 and 0.05 from horizontal walls and 0.0036 and 0.025 from the top of the obstacle. On the forward-facing wall, the first grid points are at Δx=0.0045 for Cases II and III and at 0.0033 and 0.025 for Cases I and IV respectively. On the backward-facing wall, the first grid points are at Δx=0.014 for Cases II and III and at 0.0045 and 0.025 for Cases I and IV respectively. The grid is densely packed around the obstacle and near the channel walls and geometrically stretched in the other regions. The number of control volumes in the x, y, and z directions are $112 \times 48 \times 40$ for Cases II and III, $272 \times 64 \times 64$ for Case I, and $96 \times 32 \times 32$ for Case IV. Grid refinement shows that the spatial resolution is adequate; using more control volumes shows improvement, but the difference is insignificant.

In all cases, periodic boundary conditions were employed in the homogeneous (z) direction. At the walls, no-slip boundary conditions were imposed except for Case IV where a wall-layer model was employed. We also apply periodic boundary conditions in the x direction in order to avoid any uncertainty related to outflow boundary condition which has been an area of controversy and to assure a reasonable

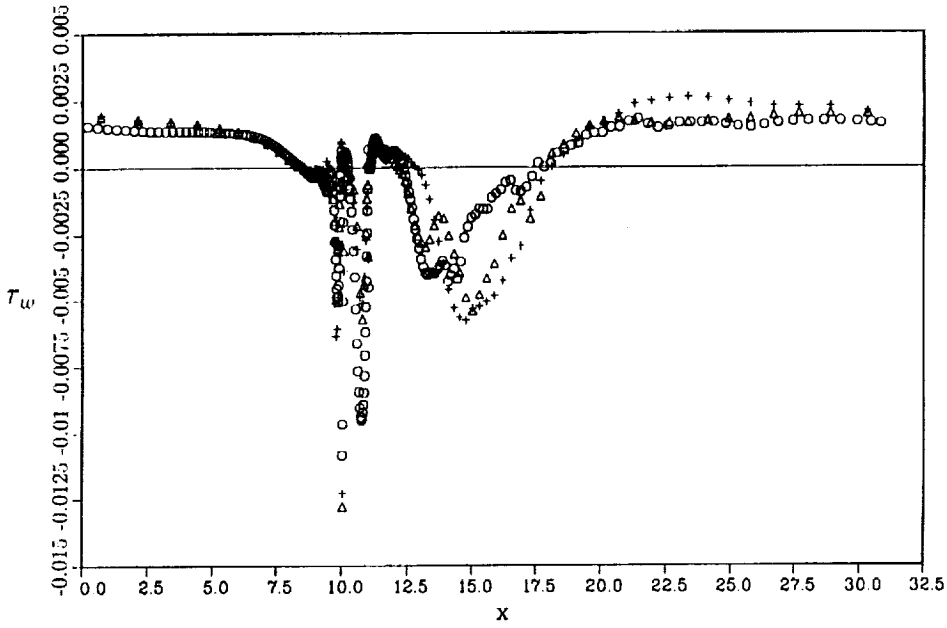

FIGURE 3(a). Averaged wall shear stress at the lower wall: o, DNS; $\triangle$, LES with DSGSM; +, LES with C_s=0.01.

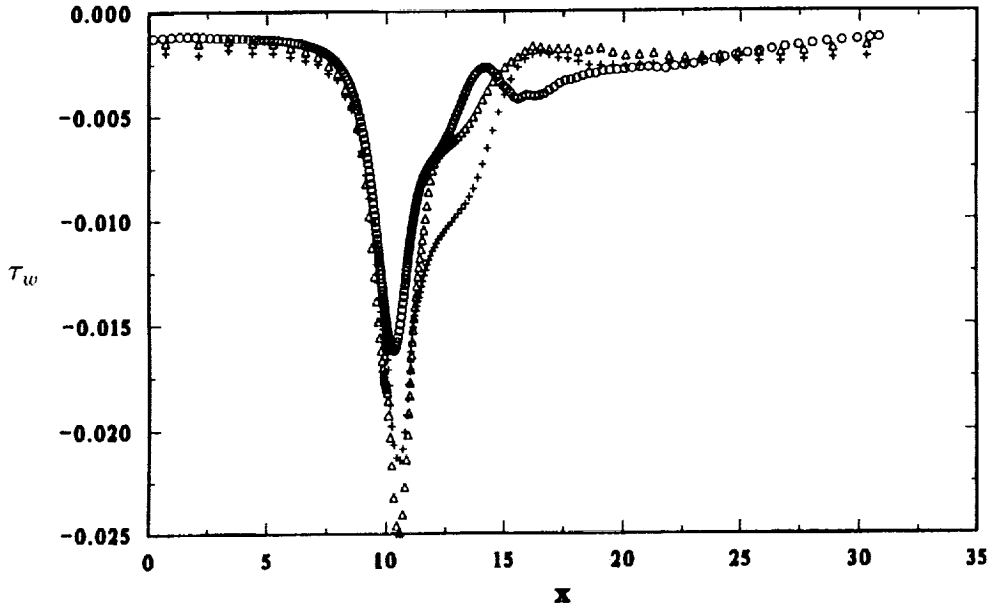

FIGURE 3(b). Averaged wall shear stress at the upper wall: o, DNS; $\triangle$, LES with DSGSM; +, LES with C_s=0.01.

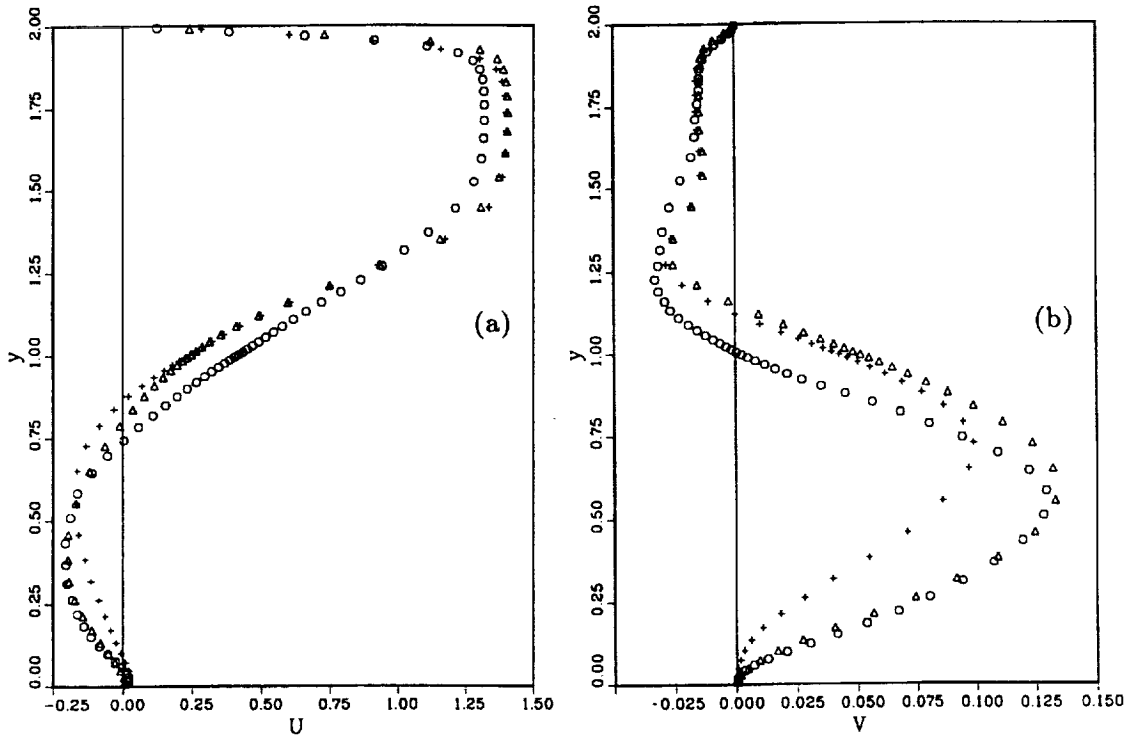

FIGURE 4. Averaged velocity profiles at x=12; (a) streamwise (U), (b) normal (V): o, DNS; $\triangle$, LES with DSGSM; +, LES with C_s=0.01.

flow approaching the obstacle. Therefore, we are actually simulating an infinitely-long channel flow with a periodic array of obstacles. To minimize the interaction between "neighboring" obstacles, the long streamwise computational domain ($31h$) is employed.

Since the pressure difference between the inlet and the outlet is fixed, Re is slightly different in each case. To match the Reynolds numbers of the various cases as closely as possible, we adjusted the pressure difference slightly. The second column of Table 1 shows Re for each low-Re case. The 3% variation in Re should be kept in mind in the comparisons below. The high-Re case will also be compared with the experiment of Dimaczek *et al.* (1989) at slightly different Re (Re=84,000). After an initial transient period, the flow becomes fully turbulent and sustained. Then, an averaging is performed in the homogeneous direction and in time in order to obtain averaged quantities. The time-averaging was taken over 27 characteristic time units (h/U_m) for low-Re cases and 38 units for Case IV.

4.2 Averaged flow field at Re=3210

The flow develops several separation and reattachment (SR) zones near the obstacle. Figure 2 shows schematic contours of U=0 (U and V represent averaged

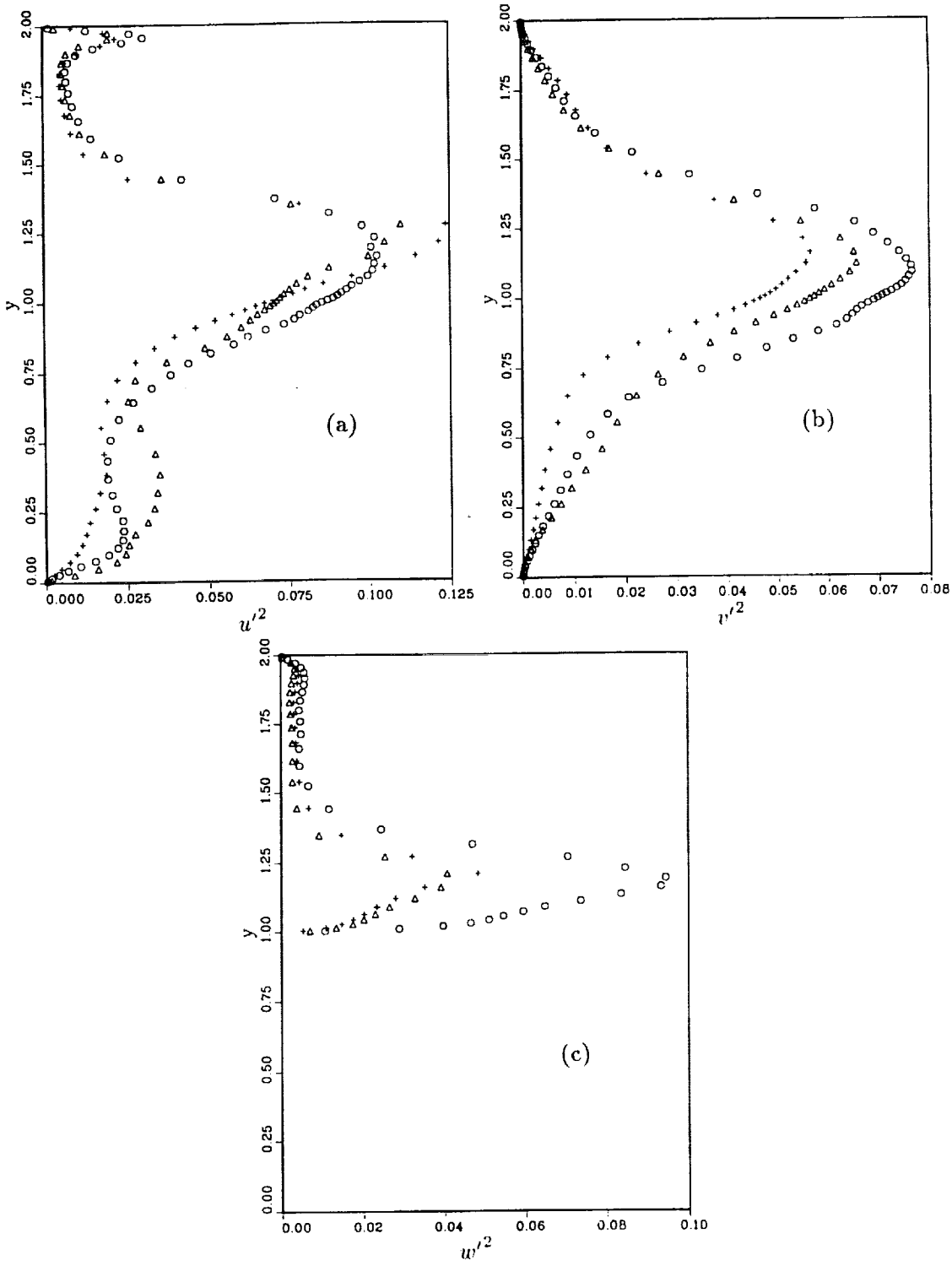

FIGURE 5. Averaged turbulent fluctuation profiles; (*a*) streamwise (u'^2) at x=12, (*b*) normal (v'^2) at x=12, (*c*) spanwise (w'^2) at x=11: ○, DNS; △ , LES with DSGSM; +, LES with C_s=0.01.

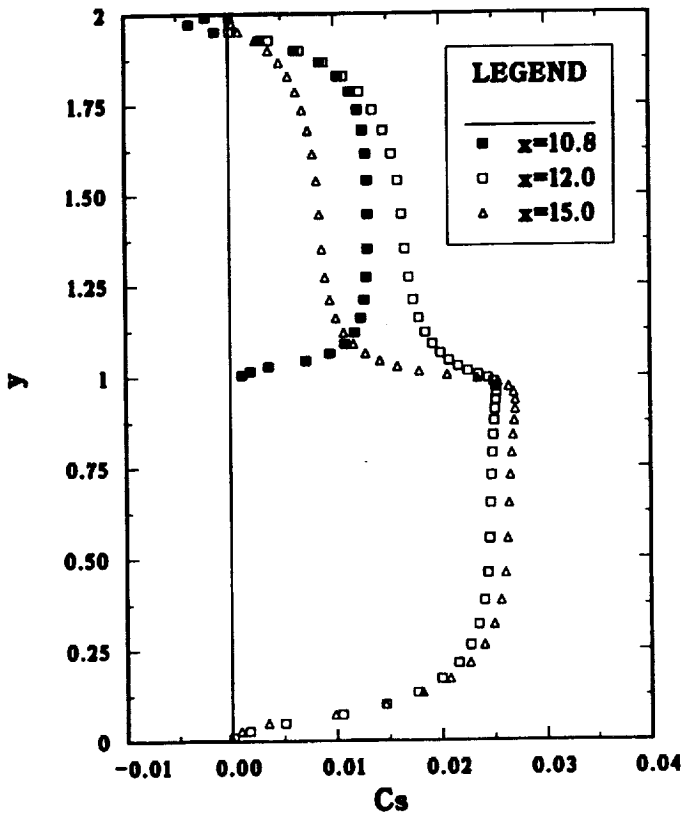

FIGURE 6. Profiles of C_s.

values of u and v, respectively). The + and − signs indicate regions of positive and negative U, respectively. In addition to the primary SR zones upstream (PSRU) and downstream (PSRD) of the obstacle, there are secondary SR zones upstream (SSRU, at the front corner), and downstream (SSRD, near the rear corner, bigger than SSRU) of the obstacle. A tertiary SR zone is discernible at the downstream corner of the obstacle (TSRD). For the given geometry and Re, reattachment does not occur on top of the obstacle in any of the three low-Re cases. The reattachment length of PSRD is denoted by X_R. The separation length and reattachment length of PSRU are represented by X_F and Y_F, respectively, and those of SSRD by X_r and Y_r, respectively. Table 1 gives computed values of those lengths in units of h for each case. Case I, the DNS, is the most accurate simulation. Its X_R differs by roughly 5% from the value of 6.1 determined in the experiment of Tropea & Gackstatter (1985). Although the aspect ratio (L/h) of the experimental obstruction is somewhat larger than in the simulation, the DNS value of X_R falls within the range of experimental error (quoted as 6%). Tropea & Gackstatter did not report other SR lengths. Case II is significantly more accurate than Case III for every length scale.

Figure 3 presents nondimensionalized shear stress (τ_w) on the lower (Fig. 3(a)) and upper walls (Fig. 3(b)). In Fig. 3(a), the values of τ_w between x=10 and x=11

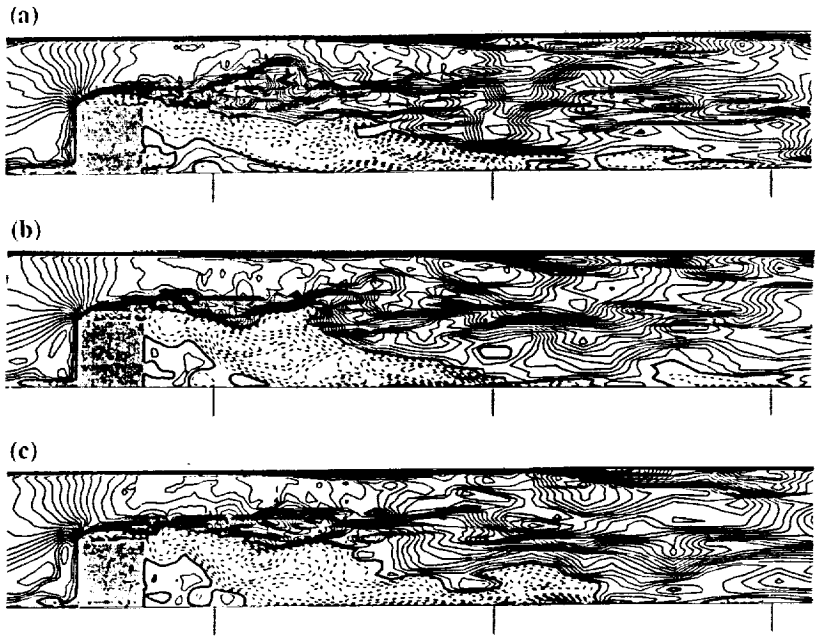

FIGURE 7. Regions of instantaneous negative u; solid, positive; dash, negative; thick solid, 0; increment, 0.016: (*a*) t=0; (*b*) t=Δt; (*c*) t=$2\Delta t$.

are for the top surface of the obstacle. The large variations in the values of τ_w on the top of the obstacle reflect the complexity of the flow in that region. The τ_w predicted by Case II agrees better with Case I in PSRD than does Case III, especially for $11 \leq x \leq 13$ and far downstream ($x \geq 20$). Case II also gives better results on the upper channel wall (Fig. 3(*b*)). The large $|\tau_w|$ near x=10 is caused by flow acceleration due to the sudden contraction in flow passage. Better agreement for $11 \leq x \leq 15$ and in the "channel region" ($x \leq 7.5$ or $x \geq 25$) are also noticeable.

Profiles of U and V at a selected streamwise location (x=12, just downstream of the obstacle) are shown in Figs. 4(*a*) and Fig. 4(*b*), respectively. In both figures, the DSGSM gives a significant improvement over the Smagorinsky model in the reversed flow region ($y \leq 0.75$).

Profiles of averaged turbulent fluctuations in the streamwise (u'^2), normal (v'^2), and spanwise (w'^2) directions at selected streamwise locations are presented in Figs. 5(*a*), 5(*b*), and Fig. 5(*c*), respectively. It should be noted that the LES results represent only the fluctuations in the resolved (grid-scale) velocity field. The subgrid-scale contribution is small at this low Re. The dynamic model gives an overall improvement for u'^2 and v'^2, but not for w'^2.

Figure 6 shows profiles of $C_s(x, y)$ at three different streamwise locations (x=10.8, 12, 15). Obviously, C_s depends upon grid used and the type of averaging in space and time. There is a sharp gradient near y=1 where the control volumes are densely clustered to resolve the flow above the obstacle. Without an arbitrary damping function, C_s vanishes at the walls and even takes some small negative values near

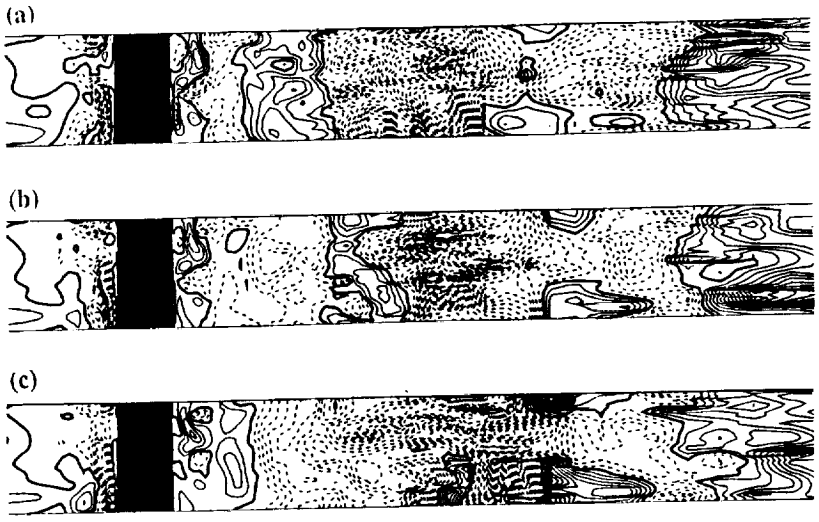

FIGURE 8. Regions of instantaneous negative u; solid, positive; dash, negative; thick solid, 0; increment, 0.016: (*a*) t=0; (*b*) t=Δt; (*c*) t=2Δt.

the upper wall.

4.3 Instantaneous flow field at Re=3210

4.3.1 Reversed flow regions

Figure 7 shows contours of u are presented at one x–y plane at three different times with a time interval of Δt=1.61. For convenience, the time for Fig. 7(*a*) is designated as t=0, and subsequent figures will be referred relative to that time. Figures 7(*a*)–(*c*) show how unsteady the flow is. Near the mean reattachment point of PSRD (6.8h downstream of the obstacle), u is small and oscillating in sign. Intense unsteady free-shear layers formed downstream of the obstacle are noticeable. Intermittent separation on the upper channel wall is observed near the streamwise location of mean reattachment (Fig. 7(*c*)).

Figures 8(*a*)–(*c*) show contours of u at the first grid point away from the lower channel wall at three different times. The instantaneous separation and reattachment lines are far from two-dimensional although the obstacle is geometrically two-dimensional. Secondary and tertiary flow regions are present near the obstacle at this Re and are highly unsteady.

Particle trace studies were also performed. A videotape displaying this data is available by request to the authors.

4.4 LES at Re=82,000

The wall-layer model we used is a variation of one proposed by Ciofalo and Collins (1989) for k–ϵ modeling of turbulent recirculating flows. It retains the form of the

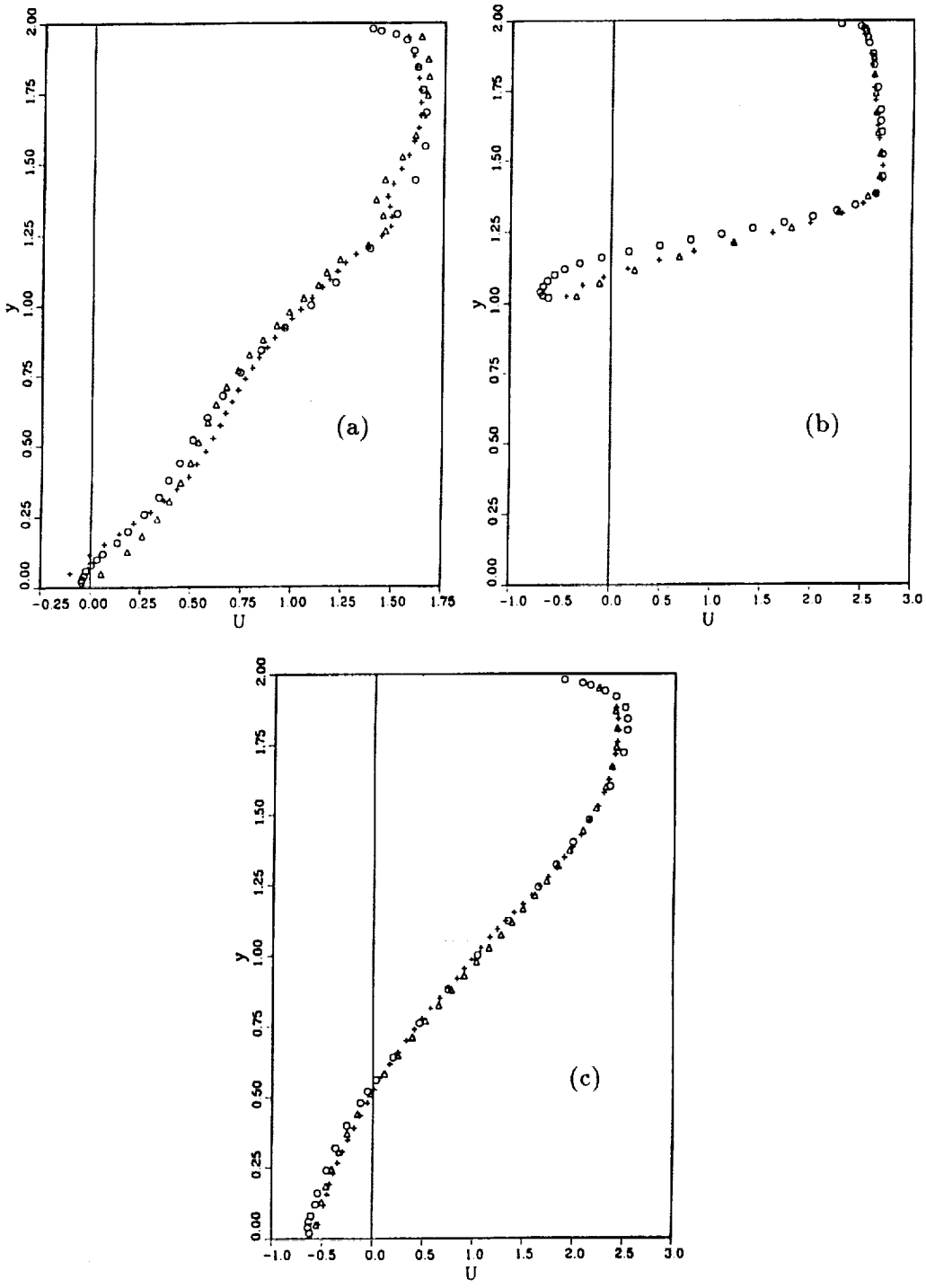

FIGURE 9. Streamwise velocity profiles: (*a*) x=9.6, (*b*) x=10.8, (*c*) x=15: ○, exp.; △ , 96x32x32; +, 128x48x40.

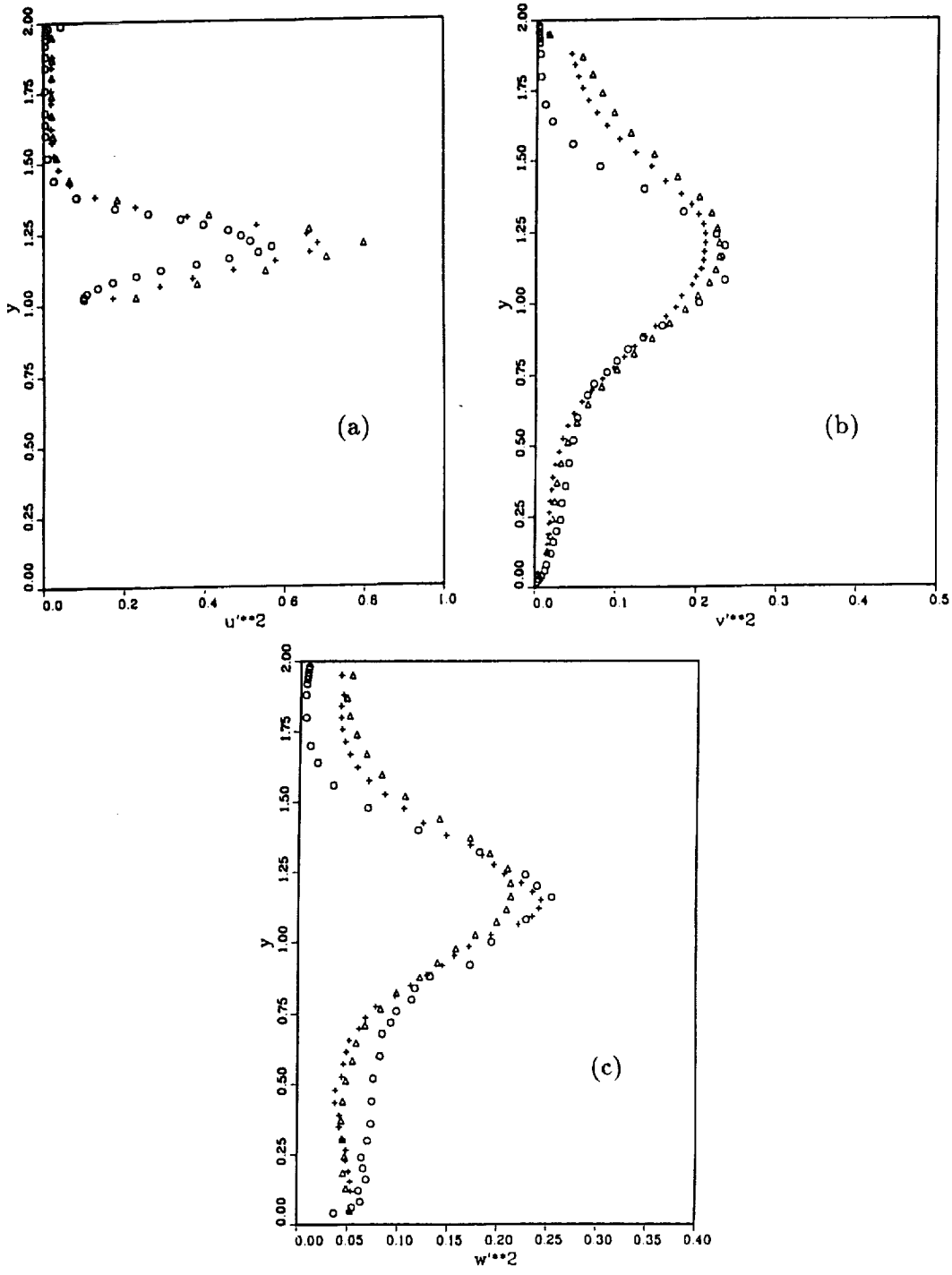

FIGURE 10. Turbulent fluctuation profiles: (*a*) u'^2 at x=10.8, (*b*) v'^2 at x=12, (*c*) w'^2 at x=12: : ○, exp.; △ , 96x32x32; +, 128x48x40.

wall function but allows the nondimensional thickness of the viscous sublayer to be a function of the local turbulence intensity.

Figure 9 presents streamwise velocity profiles normalized by $2U_m$ and averaged in z and t at three streamwise locations. Velocity profiles from coarse ($96 \times 32 \times 32$) and fine ($128 \times 48 \times 40$) grid simulations are shown along with the experimental one. The profiles are relatively well resolved. Only a slight improvement is obtained on the fine grid. The discrepancy near the top surface of the obstacle (Fig. 9(b)) is believed to be due to the wall-layer model. Averaged and normalized velocity fluctuations at selected x locations are shown in Fig. 10. Numerical results predicts higher values in the high speed regions near the upper wall.

5. Summary

A large-eddy simulation of low-Reynolds-number turbulent flow in a channel with a two-dimensional obstacle on one wall was presented with the wall layers fully resolved. The subgrid-scale model coefficient was computed dynamically. The results obtained were compared with a DNS and showed that the dynamic model yields better results than conventional LES with a fixed model constant. This demonstrates the value of the dynamic subgrid-scale model for computing complex flows. A high-Reynolds-number LES using a conventional Smagorinsky model with a fixed model constant was also included. The results are consistent with the experiment of Dimaczek *et al.* (1989). Application of the dynamic subgrid-scale model to high-Re flows is currently under investigation.

Acknowledgment

The authors gratefully acknowledge contributions from the following organizations. Financial support for the investigators was provided through the Office of Naval Research grant N00014-89J-1343 and the Stanford-NASA Center for Turbulence Research. The NASA–Ames Research Center has provided the computer time for this research.

REFERENCES

CIOFALO, M., & COLLINS, M. W. 1989 *Numerical Heat Transfer Part B.* **15,** 21-47.

DIMACZEK, G., KESSLER, R., MARTINUZZI, R., & TROPEA, C. 1989 The flow over two-dimensional, surface-mounted obstacles at high Reynolds numbers. *Proc. 7th Symposium on turbulent shear flows.* Stanford University, Aug. 21–23, 1989.

GERMANO, M., PIOMELLI, U., MOIN, P., & CABOT, W. H. 1991 A dynamic subgrid-scale eddy viscosity model. *Phys. Fluids A.* **3,** 1760-1765.

KIM, J., & MOIN, P. 1985 Application of a fractional-step method to incompressible Navier-Stokes equations. *J. Comp. Phys.* **59,** 308-323.

LILLY D. K. 1992 A proposed modification of the Germano subgrid-scale closure method. *Phys. Fluids A.* **4 (3),** 633-635.

ROBINSON, S. K., KLINE, S. J., & SPALART, P. R. 1988 Spatial character and time evolution of coherent structures in a numerically simulated boundary layer. *AIAA paper No. 88-3577.*

SHAANAN, S., FERZIGER, J., & REYNOLDS, W. 1975 Numerical simulation of turbulence in the presence of shear. *Report TF-6.* Thermosciences Division, Dept. of Mech. Eng., Stanford Univ., Stanford CA 94305, U.S.A.

SMAGORINSKY, J. 1963 General circulation experiments with the primitive equations. I. The basic experiment. *Monthly Weather Review.* **91,** 99-164.

TROPEA, C., & GACKSTATTER, R. 1985 The flow over two-dimensional surface-mounted obstacles at low Reynolds numbers. *J. Fluids Eng.* **107,** 489-494.

WERNER, H., & WENGLE, H. 1989 Large-eddy simulation of turbulent flow over a square rib in a channel. *Proc. 7th Symposium on turbulent shear flows.* Stanford University, Aug. 21–23, 1989.